Seven-layered 2D Hybrid Lead Iodide Perovskites

Lingling Mao, Rhys M. Kennard, Boubacar Traore, Weijun Ke, Claudine
Katan, Jacky Even, Michael L Chabinyc, Constantinos C Stoumpos, Mercouri
G Kanatzidis

Seven-layered 2D Hybrid Lead Iodide Perovskites

Lingling Mao[1], Rhys M. Kennard[2], Boubacar Traore[3], Weijun Ke[1], Claudine Katan[3], Jacky Even[4], Michael L. Chabinyc[2], Constantinos C. Stoumpos[1]** and Mercouri G. Kanatzidis[1]*

[1]Department of Chemistry, Northwestern University, 2145 Sheridan Road, Evanston, IL 60208 United States
[2]Materials Department, University of California, Santa Barbara, California 93106, United States
[3]Univ Rennes, ENSCR, INSA Rennes, CNRS, ISCR (Institut des Sciences Chimiques de Rennes), UMR 6226, Rennes F-35000, France
[4]Univ Rennes, INSA Rennes, CNRS, Institut FOTON, UMR 6082, Rennes F-35000, France
*Correspondence: m-kanatzidis@northwestern.edu
**Correspondence: cstoumpos@materials.uoc.gr

SUMMARY

Two-dimensional hybrid halide perovskites offer high chemical versatility, strong potential in optoelectronic applications. Here, we report the highest layer thickness yet to be crystallographically characterized, for the Dion-Jacobson (DJ) family. The seven-layered DJ phase $(4AMP)(MA)_6Pb_7I_{22}$ (4AMP = 4-aminomethylpyperidinium) shows much less distortion in the crystal structure, than the corresponding Ruddlesden-Popper (RP) phase $(BA)_2(MA)_6Pb_7I_{22}$ (BA = butylammonium). The comparison of the DJ and RP perovskites reveals that the fine structural details still influence the optical properties, with the DJ phase maintaining a lower energy absorption edge and photoluminescence emission (1.53 eV, 1.70 eV) than the RP phase (1.57 eV, 1.74 eV). Density Functional Theory (DFT) calculations show the localized density of states of conduction band minimum and valence band maximum are situated at different parts of the layers of the DJ phase and RP phase, implying separate channels in the structure followed by electrons and holes. Unlocking the high layer thickness 2D halide perovskites provides accessibility to new perovskites for high-performance optoelectronics.

INTRODUCTION

Two-dimensional (2D) halide perovskites possess huge potential in optoelectronics.[1-9] Following the success of 3D perovskites in achieving record power conversion efficiency (PCE) of over 23.7%,[10] the 2D materials have demonstrated higher stability with decent performance of 12-15% and when combined with 3D perovskites allow for considerably more device stability while maintaining high conversion efficiency.[4,11-15] From a structural perspective, the 2D perovskites are more versatile than 3D perovskites, with a general formula of $(A')_m(A)_{n-1}B_nX_{3n+1}$ where A' is a large organic spacing cation, A is a perovskitizer (methylammonium (MA^+) or formamidinium (FA^+) or Cs^+),[16] B is a metal (Pb^{2+}, Sn^{2+} etc.) and X is a halide (Cl^-, Br^-, I^-). The two main classes of multilayered 2D halide perovskites are the Dion-Jacobson (DJ)[17] and Ruddlesden-Popper (RP) phases,[18] which are defined by the charge of the interlayer spacing cation.[19] Secondary classes include the alternating cation (ACI)[20] and diammonium cation $(NH_3C_mH_{2m}NH_3)(CH_3NH_3)_{n-1}Pb_nI_{3n+1}$ (m = 4–9, n = 1–4) perovskites.[21] There are many reports on the low layer number (n = 1-4) of 2D perovskites,[22,23] including the DJ series with 3-aminomethylpiperidinium (3AMP) and 4-aminomethylpiperidinium (4AMP) (n = 1 - 4).[17] The 2D perovskites as a family are considered as natural quantum well materials in which the inorganic slabs are the semiconductor exhibit varying degrees of quantum confinement defined by the value of n and the organic spacers serving as the dielectric barriers. Currently, crystallographically characterized higher layer thickness members (n > 5) have only been reported for the RP series with butylammonium (BA) cations (n = 6 - 7),[24] In addition to having led to efficient and more stable solar cells, these higher n value materials bridge the gap between thin layered perovskites and the three-dimensional (3D) $MAPbI_3$ and their properties will help understand those of the two extremes. Because of the progressive weakening of quantum confinement with increasing layer thickness, they also offer significant benefits in photovoltaics because of lower exciton binding energies. [25] It is still an open question up to which thickness the perovskite layers may grow before losing their periodically ordered structure and convert to a bulk 3D perovskite. The limited availability of high n 2D perovskite compounds and the outstanding questions mentioned above prompted us to explore this direction further.

Here, we report on the synthesis and characterization of the thickest layered 2D perovskites (n = 7) to date demonstrated by the DJ phase $(4AMP)(MA)_6Pb_7I_{22}$ (4AMP = 4-aminomethylpyperidinium), and compare its properties with the just reported RP perovskite $(BA)_2(MA)_6Pb_7I_{22}$ (BA = butylammonium) with a detailed structural analysis.[24] The distortion levels of the crystal structures, which is a key property-defining aspect in these materials, are evaluated based on the Pb-I-Pb angles (distortion across the layers), bond angle variance (BAV) and distortion index (DI) (distortion of individual octahedron). Density Functional Theory (DFT) calculations taking into account these distortions point out the intrinsic differences in the electronic structure, where opposite

localized density of states (LDOS) in the conduction band minimum (CBM) and valence band maximum (VBM) are observed. Local inclusions of lower n phases identified via single crystal X-Ray Diffraction and visualized via
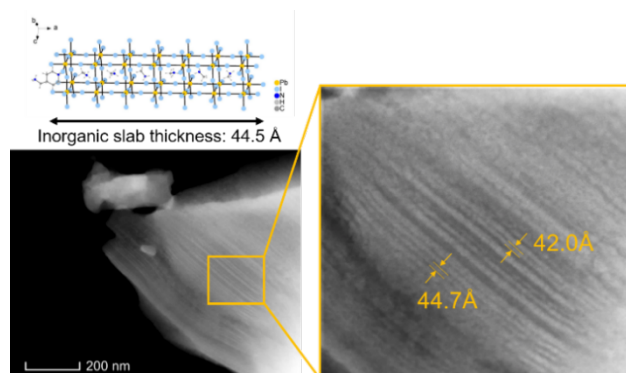

Figure 2. STEM-HAADF image of DJ phase $(4AMP)(MA)_6Pb_7I_{22}$. Zoom-in regions of the image shows clear 2D characteristics of the layered perovskite.

Scanning Transmission Electron Microscopy suggest an upper limit on possible n thickness that can be obtained in a phase-pure manner. The intricate crystal structure and its association with the optical and electronic properties provide an analytical guidance in the understanding of the high-layer-thickness compounds.

RESULTS AND DISCUSSION

The synthesis of the n = 7 DJ phase is similar to the previous report of lower layer number, [17] but with reduced 4AMP input and hydroiodic acid. An amount of 892 mg (4 mmol) 99.9% PbO powder was dissolved in 4 mL of hydroiodic acid and 0.5 mL hypophosphorous acid solution by heating under stirring for 5-10 min at 130°C until the solution turned to clear bright yellow. 636 mg (4 mmol) of methylammonium iodide (MAI) was added directly to the above solution under heating. 0.5 mL hydroiodic acid was added to 23 mg (0.2 mmol) 4AMP in a separate
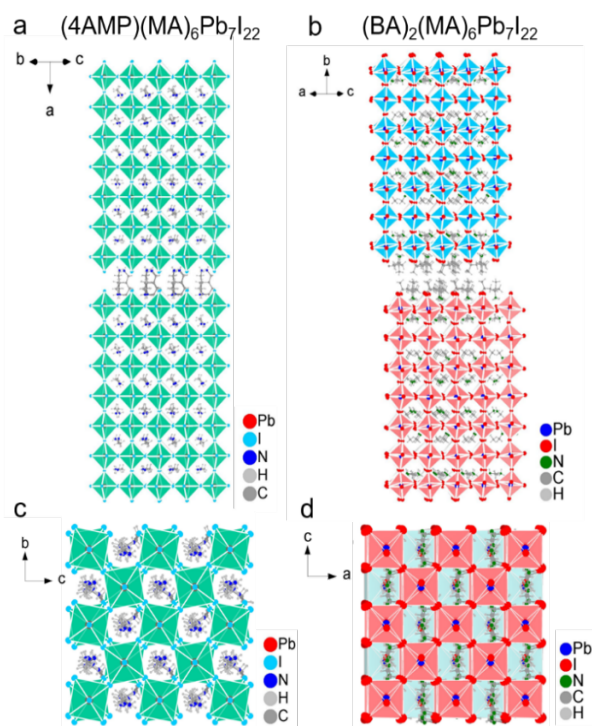

Figure 1. Crystal structure of (a) DJ phase $(4AMP)(MA)_6Pb_7I_{22}$ and (b) RP phase $(BA)_2(MA)_6Pb_7I_{22}$. Top-down view of the layers in (c) $(4AMP)(MA)_6Pb_7I_{22}$ and (d) $(BA)_2(MA)_6Pb_7I_{22}$. The layers of DJ perovskite lay on top of each other, whereas the RP phase shows an offset shifting of one octahedral unit.

vial under stirring. The protonated 4AMP solution was added into the previous solution under heating and stirring for 5-10 min. Black plate-like crystals precipitated during slow cooling to room temperature. Yield 312 mg (12.0% based on total Pb content). Powder X-ray diffraction (PXRD) shows the signature basal Bragg peaks of the n = 7 phase at ~12.7° and ~14.6°, which correspond to the (700) and (800) planes, respectively (Figure S1). The low

angle basal Bragg peaks (<10°) are not visible because their intensity is very weak. A minor n= 5 impurity can be found in the sample, similar to the previously reported n = 7 RP phase, where n = 5 and 6 impurities co-crystallize because the thermodynamic instability of the 2D phases was found to decrease with increasing n.[24]

Having evaluated the phase purity of our *n* = 7 DJ crystals, we now compare the *n* = 7 DJ phase to its analog n = 7 RP phase. The crystal structures of DJ and RP phases are shown in Figure 1. Both compounds consist of massive unit cells of ~5nm (taking unit cell centering into account), featuring inorganic perovskite layers of ~4.5 nm. The difference in the layer conformation between the two structures is clearly seen in the side view and top-down view of the structures, where the layers of DJ phase overlap exactly on top of each other, showing

Table 1. Single-crystal X-ray diffraction refinement details for the DJ phase $(4AMP)(MA)_6Pb_7I_{22}$.

Empirical formula	$(C_6N_2H_{16})(CH_3NH_3)_6Pb_7I_{22}$
Formula weight	4550.74
Temperature, wavelength	293(2) K, 0.71073 Å
Space group	*Pc*
Unit cell dimensions	a = 48.605(10) Å,
	b = 8.8635(18) Å,
	c = 8.8638(18) Å,
	β = 90.13(3)°
Volume	3818.6(13) Å^3
Density (calculated)	3.958 g/cm^3
θ range, completeness to θ = 26.000°	2.298 to 29.253°, 91.1%
Reflections collected, independent	23035, 14637 [R_{int} = 0.1065]
Data / restraints / parameters	14637 / 32 / 342
Goodness-of-fit	1.032
Final R indices [I > 2σ(I)]	R_{obs} = 0.1196,
	wR_{obs} = 0.3400

$R = \Sigma||F_o|-|F_c|| / \Sigma|F_o|$, $wR = \{\Sigma[w(|F_o|^2 - |F_c|^2)^2] / \Sigma[w(|F_o|^4)]\}^{1/2}$ and $w=1/[\sigma^2(Fo^2)+(0.2000P)^2]$ where $P=(Fo^2+2Fc^2)/3$

a (0, 0) displacement. The layers of the RP phase are more flexible showing a (1/2, 0) displacement because of the monovalent cation BA that only attaches to one side of the slab (Figure 1c-d). The interlayer space requires two sheets of organic cations of BA (singly protonated $-NH_3^+$) whereas the DJ phase only requires one sheet of the dication 4AMP (doubly protonated, $-NH_3^+$ and $-NH_2^+$). The latter locks in place the relative positions of adjacent inorganic slabs. Due to the asymmetric nature of the 4AMP cation, $(4AMP)(MA)_6Pb_7I_{22}$ crystallizes in the non-centrosymmetric monoclinic space group *Pc*, whereas the RP phase, adopts the non-centrosymmetric orthorhombic space group $C2cb$.[24] The crystallographic data and refinements details of the DJ phase is given in Table 1. To better illustrate the subtle differences in the two crystal structures, we dissect the structures into individual slabs, where each slab is a representative unit from which the whole structure is composed.

Our preliminary results of direct imaging of the inorganic slabs are shown in Figure 2. Scanning Transmission Electron Microscopy images (STEM) of an n = 7 crystal revealed stacked layers of high and low contrast (Figure 2). The high-contrast (bright) layers consistently exhibited thicknesses of 42-45 Å, which roughly matches the thickness of the Pb-I inorganic slab of the *n* = 7 (44.5 Å). Lower-contrast (darker) layers were intercalated irregularly between the high-contrast layers, suggesting the presence of a lower-Z impurity growing between layers of *n* = 7. This was consistent with the observation of *n* = 5 impurities via single-crystal XRD, as lower-*n* layers would have a higher proportion of organic cation vs. Pb. We thus interpret the lower-contrast layers to be these *n* < 7 impurities. In contrast, in low-*n* (n = 3, or n = 4) spin-coated RP thin films, impurities consisting of both lower-*n* and higher-*n* RP phases were tightly interwoven with the dominant stoichiometric phase.[26] This suggests that the nature of impurity intergrowth, whether as full, separate layers, or as interwoven crystallites, may depend on the average *n*, on the bulkiness of the large organic cation, or on the growth kinetics.

In Figure 3a-b, the n=7 inorganic slabs of the DJ phase and RP phase are placed horizontally, with individually labeled Pb-I-Pb angles. The Pb-I-Pb angle can be viewed as a parameter that quantifies the distortion across the Pb/I inorganic framework. The overall average of the Pb-I-Pb angles is 169.9º for the DJ phase and 165.1º for the RP phase. The main contribution that raises the average for the DJ phase comes from the axial Pb-I-Pb angles (perpendicular to the layers, parallel to stacking a-axis) as seen in Figure 3a, 3g and 3h, which approach the ideal 180º. The axial angles in the RP phase are all below 170º (Figure 3b, h). The other type of Pb-I-Pb angle is the equatorial Pb-I-Pb angles as defined in Figure 3g, and they extend along the infinite 2D planes. The averaged equatorial angle for the RP is larger than that for the DJ phase (163.7º vs. 160.8º), which shows a smaller in-plane distortion in the RP phase.

To consider the distortion level at the individual $[PbI_6]$ octahedron, bond angle variance (BAV) (equation 1) and distortion index (DI) (equation 2) are important parameters as they show the deviation from the perfect octahedron and provide another sense of the flexibility of the structure.
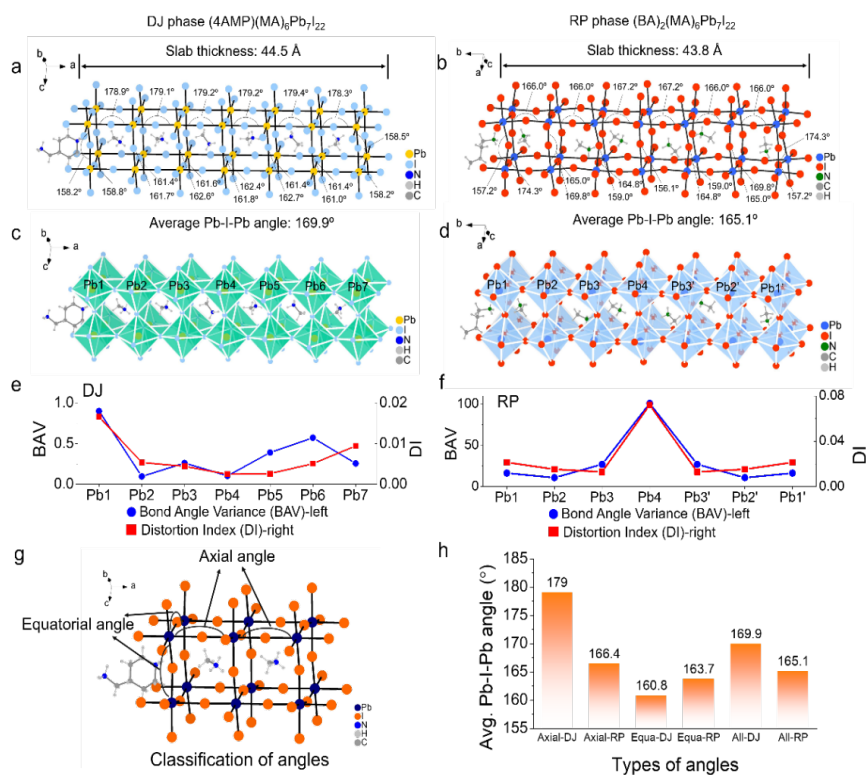
Figure 3. Detailed Pb-I-Pb angles for (a) DJ phase $(4AMP)(MA)_6Pb_7I_{22}$ and (b) RP phase $(BA)_2(MA)_6Pb_7I_{22}$. Crystallographic independent Pb environments in (c) $(4AMP)(MA)_6Pb_7I_{22}$ and (d) $(BA)_2(MA)_6Pb_7I_{22}$. (e,f) Distortion evaluation of individual $[PbI_6]$ octahedron using bond angle variance (BAV) and distortion index (DI) calculated by Vesta software. The DJ phase shows a much lower distortion level than the RP phase both on BAV and DI. (g) Classification of axial (perpendicular to the layers) and equatorial (along the layers) Pb-I-Pb angles. (h) Comparison between averaged axial, equatorial and total Pb-I-Pb angles.

$$\sigma^2 = \frac{\sum_{i=1}^{m}(\theta_i - \theta_0)^2}{m-1} \quad (1)$$

where m is (number of faces in the polyhedron) × 3/2 (i.e. number of bond angles), θ_i is the ith bond angle, and θ_0 is the ideal bond angle for a regular polyhedron (90º for an octahedron).[27]

$$D = \frac{1}{n}\sum_{i=0}^{n}\frac{|l_i - l|}{l} \quad (2)$$

where l_i is the distance from the central atom to the ith coordinating atom, and l is the average bond length.[28] We have labeled the individual $[PbI_6]$ octahedron in Figure 3c-d. In the structure of $(4AMP)(MA)_6Pb_7I_{22}$ each Pb environment is different from Pb1 to Pb7 as shown in Figure 2c. While for the RP phase because of a glide plane sitting in the middle of the layer, Pb1, Pb2 and Pb3 are equivalent to Pb1', Pb2' and Pb3' (Figure 3d).

The bond angle variance (BAV, quantifying the distortion from I-Pb-I angles inside the $[PbI_6]$) and distortion index (DI, quantifying the distortion from Pb-I bond length) are calculated using the VESTA software and listed in Table 2.[29] The BAV values of all the $[PbI_6]$ units in the DJ phase are below 1, contrary to the BAV values which are ~20 and can reach values as high as 100 for the symmetry independent layer (defined by Pb4) of the RP phase. The DI difference is less pronounced, but still the DJ phase has smaller values (0.01-0.02) and the RP phase can go as high as 0.08, clearly seen in Table 2. The smaller degree of distortion in the DJ structure suggests that the thicker 2D perovskite structures are much less strained in the DJ motif compared to the RP motif, which is a good indicator that it will be easier to construct thicker slabs (n>7) in the DJ case.

The difference in the relative strain and distortion between the DJ and RP n = 7 structures can be understood as deriving from the different influence exerted from the soft organic layers. In the DJ structure, it is the $[PbI_6]$ unit (Pb1) next to the piperidinium ring that is the most distorted and "absorbs" most of the cation-induced strain. For the RP structure on the other hand, it is the rigid middle inorganic layer $[PbI_6]$ unit (Pb4) that plays this role and therefore the lattice strain cannot be efficiently relieved in the individual layers leading to the pronounced distortion in the whole layer. The difference is caused by the inherent properties of the organic spacing cations. In RP perovskites, each layer is "individual", fully charge-balanced with electrostatically interacting monolayer of BA cations. These then stack with the other layers only through weak dispersion forces between the alkyl chain tails of the BA cations. For the DJ systems, because of the ditopic function the 4AMP dications, the stacked layers are held together through strong electrostatic forces of the two different ammonium end-groups which themselves are linked with covalent C-C bonds. This arrangement seems to work as cushion to relieve the strain in the individual perovskite layers.

Table 2. Local distortion level of the crystal structure quantified by the bond angle variance (BAV) and distortion index (DI) of the individual octahedron $[PbI_6]$.

DJ	BAV	DI	RP	BAV	DI
Pb1	0.901	0.017	Pb1	16.326	0.021
Pb2	0.980	0.005	Pb2	10.837	0.015
Pb3	0.263	0.004	Pb3	27.021	0.013
Pb4	0.105	0.003	Pb4	100.851	0.072
Pb5	0.391	0.003	Pb3'	27.021	0.013
Pb6	0.573	0.003	Pb2'	10.837	0.015
Pb7	0.258	0.009	Pb1'	16.326	0.021

The optical properties match the trend where a less distorted perovskite structure will lead to a smaller band gap.[30,31] From UV-vis absorption and steady-state PL spectra (Figure 4a-b), it is evident that the DJ phase has lower absorption edge (1.53 eV) than the RP phase, and lies between the 3D perovskite $MAPbI_3$ (1.50 eV) and the RP phase (1.57 eV). The PL emission energies for the DJ and RP phase are blue shifted from $MAPbI_3$ (1.60 eV), at 1.70 eV and 1.74 eV, respectively. By comparison, for the n = 5 case, the PL emission energy is 1.83 eV for the RP phase and 1.79 eV for the DJ phase.[17,32] A major difference in n = 7 compared with the thinner layer RP and DJ phases can
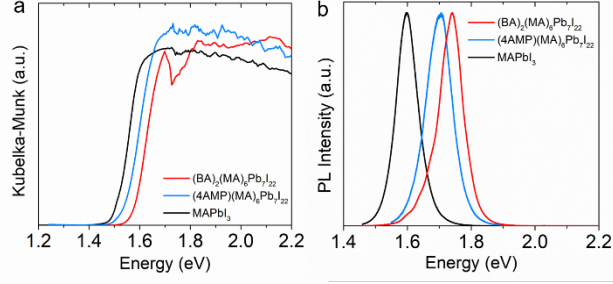
Figure 4. (a) Comparison of the optical absorption spectra and (b) steady-state photoluminescence spectra of $(4AMP)(MA)_6Pb_7I_{22}$, $(BA)_2(MA)_6Pb_7I_{22}$ and 3D $MAPbI_3$.
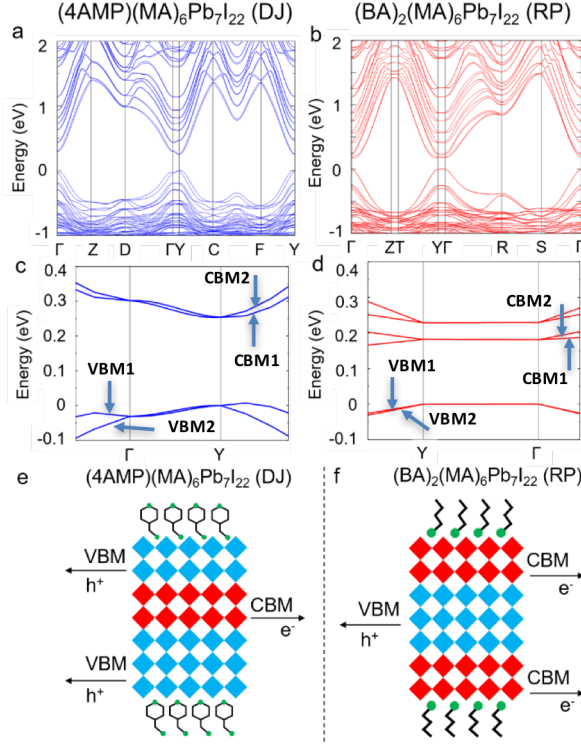

Figure 5. Comparison of the band structures of (a) $(4AMP)(MA)_6Pb_7I_{22}$ and (b) $(BA)_2(MA)_6Pb_7I_{22}$ including spin-orbit coupling effects. The zoom-in regions at the band edges show different level of dispersion, where the DJ phase has larger dispersion (c) than the RP phase (d). Schematic illustration of the localized density of states (LDOS) of conduction band minimum (CBM) and valence band maximum (VBM) in DJ phase (e) and RP phase (f).

also be seen in the in the absence of resolved characteristic exciton peaks from the absorption spectra which is understood in terms of decreasing exciton binding energy. With increasing layer thickness, the inorganic: organic aspect ratio becomes increasingly larger, practically negating the effects of dielectric confinement and approximating the dielectric properties of the 3D perovskites.[33] This aspect facilitates the breakup of the excitons into free carriers.

The intrinsic differences of the n = 7 DJ phase and RP phase in their electronic structures were also investigated with Density Functional Theory (DFT) calculations based on the experimental crystal structures (Figure 5). Figure 5 compares the electronic band structures of the RP and the DJ. The direct band gaps of 0.17 eV at Γ and 0.25 eV at Y are computed for the RP and DJ phase, respectively. The absence of the inversion center coupled with the presence of a giant spin-orbit coupling in both structures induces a small Rashba spin-splitting at mainly the conduction band (CB) for RP and both the valence band (VB) and CB for DJ. The bandwidths of the CB are similar for the DJ and RP phase, while the RP phase shows a wider bandwidth of the VB than the DJ phase (~ 0.7 eV vs. 0.5 eV). We notice flat dispersions (< 1 meV) along YΓ for RP in reciprocal space, which corresponds to its stacking axis in real space, whereas for the DJ phase slight dispersions along the stacking ΓY axis (bandwidth ~31 meV at VBM and ~48 meV at CBM) are predicted at this level of theory. The small band dispersion arises from the close I···I interaction between adjacent $[Pb_7I_{22}]$ slabs brought about by the small 4AMP cations as discussed previously (Figure S5). Nevertheless, this dispersion in the DJ compound along ΓY is exaggerated due to the band gap underestimation within DFT, which largely influences the effective masses and subsequently the band dispersions.

The orbital hybridization near the VBM and CBM edges can be best seen from wave functions, computed without SOC (Figure S6). Typically, for lead iodide perovskite systems, VBM is made of an anti-bonding hybridization between Pb (6s) and I (5p) while CBM mainly consists of bonding hybridization between Pb (6p) states.[34] We note that the spatial localizations of LDOS computed with SOC are consistent with their wave function distributions on the different octahedral planes.

The localized densities of states (LDOS) at VBM and CBM for both class types show different spatial distributions (Figure 5, S7). For RP, VBM is localized at the inner octahedral layer while CBM is located at the outer octahedral planes. For DJ, CBM is mostly localized over the inner layer whereas VBM is asymmetrically localized over one side of the outer layer. The latter asymmetry can be traced back to the two different charged moieties in the 4AMP di-cations ($-NH_2^+$ versus $-NH_3^+$) that induces a net dipole (Figure S8 and Figure S9), which in turn induces the asymmetry of the electronic density distribution at VBM that localizes on the $[NH_3]^+$ side. The localization is driven by the structural properties of the inorganic framework. In the DJ case, the anti-bonding character of the VBM, causes them to localize on the layers that are more distorted (outer layers). This trend is the opposite for the RP phase, as the more distorted layers are in the middle (Figure 5e-f). The LDOS of VBM and CBM in DJ and RP phases indicates that the electron and hole pathways are distinctively different in these materials, thus different optoelectronic engineering strategies should be considered for devices.

CONCLUSIONS

The successful synthesis of the thick 2D halide perovskites $(4AMP)(MA)_6Pb_7I_{22}$ and $(BA)(MA)_6Pb_7I_{22}$ suggests that even thicker 2D perovskites approaching the bulk macroscopic scale are likely achievable. Comparing the structural distortion of the DJ and RP phases, we can see that the DJ $(4AMP)(MA)_6Pb_7I_{22}$ structure is less strained than the RP phase $(BA)(MA)_6Pb_7I_{22}$, leading broader electronic bands and lower band gap energy. Experimentally, the absorption edge and PL emission of the DJ phase lies in-between the 3D perovskite $MAPbI_3$ and the RP phase. As increasingly thicker inorganic perovskites are synthesized, we can expect these periodic 2D structures to reach dimensions similar to quantum dot nanocrystals a size regime where the barriers between the quantum and the classical world can be crossed allowing the exploration of new physics.

EXPERIMENTAL PROCEDURES

Materials. PbO (99.9%), 4-(aminomethyl)piperidine (96%), hydroiodic acid (57 wt. % in H_2O, distilled, stabilized, 99.95%) and hypophosphorous acid solution (50 wt. % in H_2O) were purchased from Sigma-Aldrich and used as received. Methylammonium iodide (>99.5%) was purchased from Luminescence Technology Corp. and used as received.

Synthesis of $(4AMP)(MA)_6Pb_7I_{22}$. An amount of 892 mg (4 mmol) 99.9% PbO powder was dissolved in 4 mL of hydroiodic acid and 0.5 mL hypophosphorous acid solution by heating under stirring for 5-10 min at 130°C until the solution turned to clear bright yellow. 636 mg (4 mmol) of methylammonium iodide (MAI) was added directly to the above solution under heating. 0.5 mL hydroiodic acid was added to 23 mg (0.2 mmol) 4AMP in a separate vial under stirring. The protonated 4AMP solution was added into the previous solution under heating and stirring for 5 min. Black plate-like crystals precipitated during slow cooling to room temperature. Yield 312 mg (12.0% based on total Pb content).

Scanning Transmission Electron Microscopy (STEM). High-angle annular dark-field (HAAFS) STEM images were acquired using a ThermoFisher Talos G2 200X TEM/STEM operating at 200 keV and $\sim$ 3 nA. n = 7 DJ crystals were crushed onto TEM grids (Ted Pella No. 01824, ultrathin C film on holey carbon support film, 400 mesh, Cu) using a razor blade.

Single Crystal X-ray Diffraction. Full sphere data were collected after screening for a few frames using either a STOE IPDS 2 diffractometer with graphite-monochromatized Mo Kα radiation (λ = 0.71073 Å) (50 kV/40 mA) under N_2 at 293 K. The collected data was integrated and applied with numerical absorption corrections using the STOE X-AREA programs. The crystal structure was solved by direct methods and refined by full-matrix least-squares on F^2 using the OLEX2 program package.[35]

Steady State Photoluminescence. Steady-state PL spectra were collected using HORIBA LabRAM HR Evolution Confocal RAMAN microscope. 473 nm laser (0.1% power) was used to excite all samples at 50× magnification.

DFT Simulations. The calculations were performed within the Density Functional Theory (DFT)[36,37] as implemented in SIESTA package[38] with a basis set of finite-range of numerical atomic orbitals. We used the Generalized Gradient Approximation (GGA) with Perdew-Burke-Ernzerhof (PBE) functional[39] to describe the exchange-correlation term, and norm-conserving Troullier-Martins pseudopotentials were used for each atomic species to account for the core electrons.[40] $1s^1$, $2s^22p^2$, $2s^22p^3$, $5s^25p^5$ and $5d^{10}6s^26p^2$ were used as valence electrons for H, C, N, I, and Pb respectively. Polarized Double-Zeta (DZP) basis set with an energy shift of 50 meV and a Mesh cutoff 200 Rydberg were used for the calculations. The Brillouin zone was sampled with 6x6x2, and 2x6x6 Monckhorst-Pack grids for $(BA)_2(MA)_6Pb_7I_{22}$ and $(4AMP)(MA)_6Pb_7I_{22}$ respectively. The densities of states (DOS) were generated with a Gaussian

smearing of 0.1 eV. The electronic properties were calculated using the experimental lattice parameters and atomic coordinates. Spin-Orbit coupling (SOC) was taken into account in the calculation of the electronic band structures.

SUPPLEMENTAL INFORMATION
Supplemental Information includes crystallographic details, powder X-ray diffraction and extra calculation details.

AUTHOR CONTRIBUTIONS
Kanatzidis, M. G., Mao, L. and Stoumpos, C. C. conceived the idea. Mao, L. conducted, designed the experiments and wrote the paper. Kennard, R. M. conducted the TEM experiments. Traore, B., Katan, C. and Even, J. conducted the DFT calculations. All authors discussed the results and wrote the paper.

DECLARATION OF INTERESTS
The authors declare no competing interests.

REFERENCES AND NOTES
1. Saparov, B., and Mitzi, D. B. (2016). Organic–inorganic perovskites: structural versatility for functional materials design. Chem. Rev. *116*, 4558-4596.
2. Chen, Y., Sun, Y., Peng, J., Tang, J., Zheng, K., and Liang, Z. (2018). 2D Ruddlesden–Popper perovskites for optoelectronics. Adv. Mater. *30*, 1703487.
3. Yuan, M., Quan, L. N., Comin, R., Walters, G., Sabatini, R., Voznyy, O., Hoogland, S., Zhao, Y., Beauregard, E. M., Kanjanaboos, P. (2016). Perovskite energy funnels for efficient light-emitting diodes. Nat. Nanotechnol. *11*, 872.
4. Tsai, H., Nie, W., Blancon, J.-C., Stoumpos, C. C., Asadpour, R., Harutyunyan, B., Neukirch, A. J., Verduzco, R., Crochet, J. J., Tretiak, S. Pedesseau, L., Even, J., Alam, M. A., Gupta, G., Lou, J., Ajayan, P. M., Bedzyk, M. J., and Kanatzidis, M. G. (2016). High-efficiency two-dimensional Ruddlesden–Popper perovskite solar cells. Nature. *536*, 312.
5. Cao, D. H., Stoumpos, C. C., Farha, O. K., Hupp, J. T., and Kanatzidis, M. G. (2015). 2D homologous perovskites as light-absorbing materials for solar cell applications. J. Am. Chem. Soc. *137*, 7843-7850.
6. Smith, I. C., Hoke, E. T., Solis-Ibarra, D., McGehee, M. D., and Karunadasa, H. I. (2014). A layered hybrid perovskite solar-cell absorber with enhanced moisture stability. Angew. Chem. Int. Ed. 53, 11232-11235.
7. Katan, C., Mercier, N., and Even, J. (2019). Quantum and Dielectric Confinement Effects in Lower-Dimensional Hybrid Perovskite Semiconductors. Chem. Rev. *119*, 3140-3192.
8. Smith, M. D., Connor, B. A., and Karunadasa, H. I. (2019). Tuning the Luminescence of Layered Halide Perovskites. Chem. Rev. *119*, 3104-3139.
9. Mao, L., Stoumpos, C. C., and Kanatzidis, M. G. (2019). Two-Dimensional Hybrid Halide Perovskites: Principles and Promises. J. Am. Chem. Soc. *141*, 1171-1190.
10. NREL's "Best Research-Cell Efficiencies" Chart. https://www.nrel.gov/pv/assets/pdfs/pv-efficiencies-07-17-2018.pdf
11. Zhou, N., Shen, Y., Li, L., Tan, S., Liu, N., Zheng, G., Chen, Q., and Zhou, H. (2017). Exploration of crystallization kinetics in quasi two-dimensional perovskite and high performance solar cells. J. Am. Chem. Soc. 140, 459-465.
12. Proppe, A. H., Quintero-Bermudez, R., Tan, H., Voznyy, O., Kelley, S. O., and Sargent, E. H. (2018). Synthetic control over quantum well width distribution and carrier migration in low-dimensional perovskite photovoltaics. J. Am. Chem. Soc. *140*, 2890-2896.
13. Ke, W., Mao, L., Stoumpos, C. C., Hoffman, J., Spanopoulos, I., Mohite, A. D., and Kanatzidis, M. G. (2019). Compositional and Solvent Engineering in Dion–Jacobson 2D Perovskites Boosts Solar Cell Efficiency and Stability. Adv. Energy. Mater. *9*, 1803384.
14. Fu, W., Wang, J., Zuo, L., Gao, K., Liu, F., Ginger, D. S., and Jen, A. K.-Y. (2018). Two-Dimensional Perovskite Solar Cells with 14.1% Power Conversion Efficiency and 0.68% External Radiative Efficiency. ACS Energy Lett. *3*, 2086-2093.
15. Zhang, F., Kim, D. H., Lu, H., Park, J.-S., Larson, B. W., Hu, J., Gao, L., Xiao, C., Reid, O. G., Chen, X., Zhao, Q., Ndione, P. F., Berry, J. J., You, W., Walsh, A., Beard, M. C., and Zhu, K. (2019). Enhanced Charge Transport in 2D Perovskites via Fluorination of Organic Cation. J. Am. Chem. Soc. *141*, 5972–5979.
16. Stoumpos, C. C., Mao, L., Malliakas, C. D., and Kanatzidis, M. G. (2017). Structure–Band Gap Relationships in Hexagonal Polytypes and Low-Dimensional Structures of Hybrid Tin Iodide Perovskites. Inorg. Chem. *56*, 56-73.
17. Mao, L., Ke, W., Pedesseau, L., Wu, Y., Katan, C., Even, J., Wasielewski, M. R., Stoumpos, C. C., and Kanatzidis, M. G. (2018). Hybrid Dion–Jacobson 2D Lead Iodide Perovskites. J. Am. Chem. Soc.*140*, 3775-3783.
18. Stoumpos, C. C., Cao, D. H., Clark, D. J., Young, J., Rondinelli, J. M., Jang, J. I., Hupp, J. T., and Kanatzidis, M. G. (2016). Ruddlesden–Popper Hybrid Lead Iodide Perovskite 2D Homologous Semiconductors. Chem. Mater. *28*, 2852-2867.
19. Tilley, R. J., (2016). Perovskites: Structure-Property Relationships. John Wiley & Sons.
20. Soe, C. M. M., Stoumpos, C. C., Kepenekian, M., Traoré, B., Tsai, H., Nie, W., Wang, B., Katan, C., Seshadri, R., Mohite, A. D., Even, J., Marks, T. J., and Kanatzidis, M. G. (2017). New Type of 2D Perovskites with Alternating Cations in the Interlayer Space, $(C(NH_2)_3)(CH_3NH_3)_nPb_nI_{3n+1}$: Structure, Properties, and Photovoltaic Performance. J. Am. Chem. Soc.*139*, 16297-16309.
21. Li, X., Hoffman, J., Ke, W., Chen, M., Tsai, H., Nie, W., Mohite, A. D., Kepenekian, M., Katan, C., Even, J., Wasielewski, M. R., Stoumpos, C. C., and Kanatzidis, M. G. (2018). Two-Dimensional Halide Perovskites Incorporating Straight Chain Symmetric Diammonium Ions, $(NH_3C_mH_{2m}NH_3)(CH_3NH_3)_{n-1}Pb_nI_{3n+1}$ (m = 4–9, n = 1–4). J. Am. Chem. Soc. *140*, 12226-12238.
22. Mitzi, D. B., Feild, C., Harrison, W., and Guloy, A. (1994). Conducting tin halides with a layered organic-based perovskite structure. Nature. *369*, 467.
23. Mitzi, D., Wang, S., Feild, C., Chess, C., and Guloy, A. (1995). Conducting layered organic-inorganic halides containing< 110>-oriented perovskite sheets. Science. *267*, 1473-1476.
24. Soe, C. M. M., Nagabhushana, G., Shivaramaiah, R., Tsai, H., Nie, W., Blancon, J.-C., Melkonyan, F., Cao, D. H., Traoré, B., Pedesseau, L., Kepenekian, M., Katan, C., Even, J., Marks, T. J., Navrotsky, A., Mohite, A. D., Stoumpos, C. C., and Mercouri G. Kanatzidis (2019). Structural and thermodynamic limits of layer thickness in 2D halide perovskites. Proc. Natl. Acad. Sci. *116*, 58-66.
25. Blancon, J.-C., Stier, A. V., Tsai, H., Nie, W., Stoumpos, C., Traore, B., Pedesseau, L., Kepenekian, M., Katsutani, F., Noe, G. (2018). Scaling law for excitons in 2D perovskite quantum wells. Nat. Commun. *9*, 2254.
26. Venkatesan, N. R., Kennard, R. M., DeCrescent, R. A., Nakayama, H., Dahlman, C. J., Perry, E. E., Schuller, J. A., and Chabinyc, M. L. (2018). Phase Intergrowth and Structural Defects in Organic Metal Halide Ruddlesden–Popper Thin Films. Chem. Mater. *30*, 8615-8623.
27. Robinson, K., Gibbs, G., and Ribbe, P. (1971). Quadratic elongation: a quantitative measure of distortion in coordination polyhedra. Science. *172*, 567-570.
28. Baur, W. (1971). The geometry of polyhedral distortions. Predictive relationships for the phosphate group. Acta Crystallogr. B Struct. Cryst. Cryst. 30, 1195-1215.
29. Momma, K., and Izumi, F. (2011). VESTA 3 for three-dimensional visualization of crystal, volumetric and morphology data. J. Appl. Crystallogr. *44*, 1272-1276.

30. Stoumpos, C. C., and Kanatzidis, M. G. (2015). The renaissance of halide perovskites and their evolution as emerging semiconductors. Acc. Chem. Res. *48*, 2791-2802.
31. Stoumpos, C. C., and Kanatzidis, M. G. (2016). Halide Perovskites: Poor Man's High-Performance Semiconductors. Adv. Mater. *28*, 5778-5793.
32. Stoumpos, C. C., Soe, C. M. M., Tsai, H., Nie, W., Blancon, J.-C., Cao, D. H., Liu, F., Traoré, B., Katan, C., Even, J. Mohite, A. D., and Kanatzidis, M. G. (2017). High members of the 2D Ruddlesden-Popper halide perovskites: synthesis, optical properties, and solar cells of $(CH_3(CH_2)_3NH_3)_2(CH_3NH_3)_4Pb_5I_{16}$. *Chem. 2*, 427-440.
33. Pedesseau, L., Sapori, D., Traore, B., Robles, R., Fang, H.-H., Loi, M. A., Tsai, H., Nie, W., Blancon, J.-C., Neukirch, A.Tretiak, S., Mohite, A. D., Katan, C., Even, J., and Kepenekian, M A (2016). Advances and promises of layered halide hybrid perovskite semiconductors. ACS nano. *10*, 9776-9786.
34. Goesten, M. G., and Hoffmann, R. (2018). Mirrors of Bonding in Metal Halide Perovskites. J. Am. Chem. Soc. *140*, 12996-13010.
35. Dolomanov, O. V., Bourhis, L. J., Gildea, R. J., Howard, J. A., and Puschmann, H. (2009). OLEX2: a complete structure solution, refinement and analysis program. J. Appl. Crystallogr. *42*, 339-341.
36. Hohenberg, P., and Kohn, W. (1964). Inhomogeneous electron gas. *Phys. Rev. 136*, B864.
37. Kohn, W., and Sham, L. J. (1965). Self-consistent equations including exchange and correlation effects. Phys. Rev. *140*, A1133.
38. Soler, J. M., Artacho, E., Gale, J. D., García, A., Junquera, J., Ordejón, P., and Sánchez-Portal, D. (2002). The SIESTA method for ab initio order-N materials simulation. J. Phys. Condens. Matter. *14*, 2745.
39. Perdew, J. P., Burke, K., and Ernzerhof, M. (1996). Generalized gradient approximation made simple. Phys. Rev. Lett. *77*, 3865.
40. Troullier, N., and Martins, J. L. (1991). Efficient pseudopotentials for plane-wave calculations. Phys. Rev. B. *43*, 1993.

SUPPORTING INFORMATION

Section S1. Experimental details.

1. *Powder X-ray Diffraction*

PXRD analysis was performed using a Rigaku Miniflex600 powder X-ray diffractometer (Cu Kα graphite, λ = 1.5406 Å) operating at 40 kV/15 mA with a Kβ foil filter.
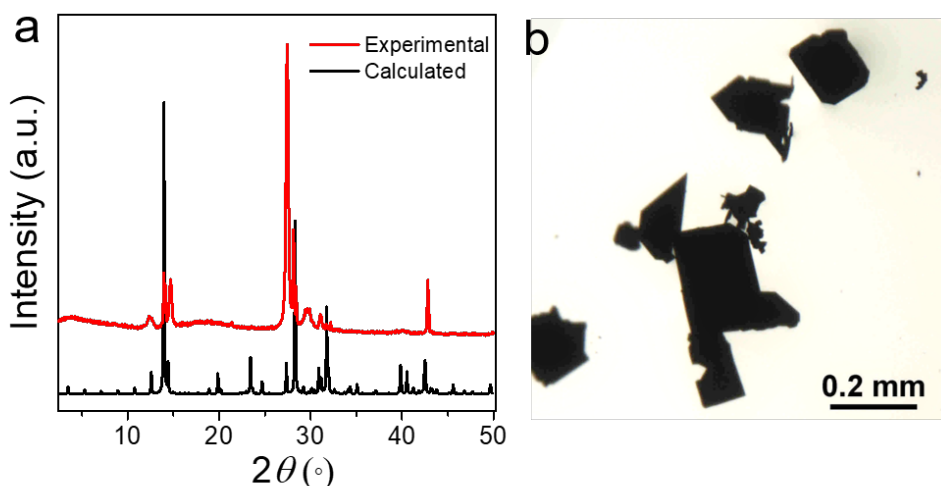
Figure S1. (a) Experimental and calculated powder X-ray diffraction (PXRD) patterns of $(4AMP)(MA)_6Pb_7I_{22}$. (b) Optical microscope picture of $(4AMP)(MA)_6Pb_7I_{22}$.

2. *Optical Absorption Spectroscopy*

Optical diffuse reflectance measurements were performed using a Shimadzu UV-3600 UV-VIS-NIR spectrometer operating in the 200 – 1000 nm region using $BaSO_4$ as the reference of 100% reflectance. The band gap of the material was estimated by converting reflectance to absorption according to the Kubelka–Munk equation: $\alpha/S = (1–R)^2(2R)^{-1}$, where R is the reflectance and α and S are the absorption and scattering coefficients, respectively.

Table S1. Atomic coordinates (x10^4) and equivalent isotropic displacement parameters (Å^{2}x10^3) for (4AMP)(MA)$_6$Pb$_7$I$_{22}$ at 293(2) K with estimated standard deviations in parentheses.

Label	x	y	z	Occupancy	U$_{eq}$*
Pb(1)	1396(2)	2499(4)	5957(5)	1	47(1)
Pb(2)	2723(1)	2494(4)	5976(4)	1	45(1)
Pb(3)	4035(1)	2499(4)	5935(4)	1	41(1)
Pb(4)	5342(2)	2500(4)	5944(6)	1	39(1)
Pb(5)	6650(1)	2498(3)	5941(4)	1	39(1)
Pb(6)	7963(1)	2491(3)	5967(3)	1	40(1)
Pb(7)	9279(1)	2493(4)	5954(5)	1	48(1)
I(1)	761(2)	2498(18)	6010(17)	1	136(5)
I(2)	1401(2)	5478(8)	3905(10)	1	80(3)
I(3)	1412(3)	474(7)	2966(10)	1	86(3)
I(4)	2081(2)	2524(10)	5993(13)	1	83(3)
I(5)	2727(2)	4584(8)	3058(11)	1	86(3)
I(6)	2722(3)	404(8)	8856(11)	1	85(3)
I(7)	3384(2)	2508(12)	5992(14)	1	98(3)
I(8)	4029(2)	4593(8)	8818(11)	1	82(3)
I(9)	4034(3)	385(8)	3051(11)	1	91(3)
I(10)	4694(2)	2502(11)	5982(13)	1	84(3)
I(11)	5341(3)	400(8)	8831(11)	1	90(3)
I(12)	5341(2)	4613(8)	3042(10)	1	77(2)
I(13)	5998(2)	2516(9)	5973(12)	1	80(2)
I(14)	6640(3)	380(8)	3039(10)	1	82(3)
I(15)	6649(2)	4585(8)	8837(10)	1	77(2)
I(16)	7302(2)	2499(9)	5981(11)	1	70(2)
I(17)	7959(2)	-412(8)	3870(10)	1	80(3)
I(18)	7953(2)	5401(8)	8037(9)	1	79(3)
I(19)	8612(2)	2542(11)	5980(13)	1	86(3)
I(20)	9267(3)	465(7)	2960(10)	1	89(3)
I(21)	9275(3)	4516(8)	8923(10)	1	82(3)
I(22)	9915(3)	2518(19)	5991(19)	1	147(6)
N(1)	923(18)	7100(120)	6040(100)	1	160(20)
H(1A)	1075	7803	5995	1	193
H(1B)	953	6335	5275	1	193
N(2)	-116(18)	6620(130)	7370(130)	1	160(20)
H(2A)	-160	6418	6415	1	193
H(2B)	-70	7584	7457	1	193

H(2C)	-260	6422	7960	1	193
C(1)	928(17)	6340(130)	7560(110)	1	160(20)
H(1C)	1079	5632	7564	1	193
H(1D)	969	7109	8307	1	193
C(2)	675(19)	5520(120)	8060(120)	1	160(20)
H(2D)	685	4492	7693	1	193
H(2E)	675	5484	9152	1	193
C(3)	409(16)	6190(130)	7540(100)	1	160(20)
H(3)	406	7045	8245	1	193
C(4)	405(17)	7090(130)	6110(120)	1	160(20)
H(4A)	257	7819	6186	1	193
H(4B)	359	6408	5294	1	193
C(5)	660(20)	7930(110)	5680(120)	1	160(20)
H(5A)	657	8123	4601	1	193
H(5B)	664	8891	6192	1	193
C(6)	122(18)	5650(120)	7840(150)	1	160(20)
H(6A)	106	5465	8913	1	193
H(6B)	102	4678	7339	1	193
N(3)	2180(30)	2000(130)	11820(120)	1	150(40)
H(3A)	2333	1469	11670	1	174
H(3B)	2043	1386	12073	1	174
H(3C)	2209	2664	12562	1	174
C(7)	2110(40)	2830(170)	10400(150)	1	150(40)
H(7A)	2269	3018	9824	1	218
H(7B)	2021	3776	10655	1	218
H(7C)	1980	2234	9817	1	218
N(4)	3490(40)	7220(160)	6690(140)	1	180(50)
H(4C)	3486	7897	7428	1	211
H(4D)	3661	6965	6479	1	211
H(4E)	3395	6401	6976	1	211
C(8)	3360(50)	7900(200)	5310(170)	1	180(50)
H(8C)	3459	7590	4437	1	263
H(8B)	3352	8953	5397	1	263
H(8A)	3171	7497	5223	1	263
N(5)	4820(20)	7750(100)	6680(90)	1	110(20)
H(5C)	4928	8536	6420	1	129
H(5D)	4931	6988	6960	1	129
H(5E)	4715	8013	7437	1	129

Label					
C(9)	4650(30)	7280(140)	5350(110)	1	110(20)
H(9A)	4771	7028	4525	1	161
H(9B)	4534	8099	5065	1	161
H(9C)	4544	6421	5623	1	161
N(6)	6060(40)	1880(170)	10240(180)	1	230(70)
H(6C)	5908	1341	10125	1	271
H(6D)	6197	1279	10554	1	271
H(6E)	6107	2293	9362	1	271
C(10)	6010(60)	3100(200)	11400(200)	1	230(70)
H(10A)	5830	3024	11772	1	339
H(10B)	6038	4069	10921	1	339
H(10C)	6143	2990	12201	1	339
N(7)	7380(50)	1980(180)	11500(200)	1	230(70)
H(7D)	7536	1482	11339	1	271
H(7E)	7238	1421	11176	1	271
H(7F)	7361	2165	12477	1	271
C(11)	7380(60)	3400(200)	10600(200)	1	230(70)
H(11A)	7479	3300	9704	1	338
H(11B)	7479	4191	11231	1	338
H(11C)	7199	3767	10449	1	338
N(8)	8690(60)	7100(200)	6200(300)	1	330(110)
H(8D)	8680	6225	6719	1	392
H(8E)	8869	7359	6148	1	392
H(8F)	8639	6855	5221	1	392
C(12)	8520(70)	8300(300)	6800(300)	1	330(110)
H(12A)	8407	8716	6028	1	490
H(12B)	8631	9037	7259	1	490
H(12C)	8399	7852	7570	1	490

[*]U_{eq} is defined as one third of the trace of the orthogonalized U_{ij} tensor.

Table S2. Anisotropic displacement parameters ($\text{Å}^2 \text{x} 10^3$) for (4AMP)(MA)$_6$Pb$_7$I$_{22}$ at 293(2) K with estimated standard deviations in parentheses.

Label	U_{11}	U_{22}	U_{33}	U_{12}	U_{13}	U_{23}
Pb(1)	62(3)	38(2)	42(2)	5(2)	9(2)	5(2)
Pb(2)	34(2)	52(2)	48(2)	13(2)	-2(2)	-4(2)
Pb(3)	40(2)	40(2)	42(2)	-2(2)	-1(2)	-5(2)
Pb(4)	42(2)	39(1)	37(1)	-1(2)	2(1)	-4(1)

Label	U_{11}	U_{22}	U_{33}	U_{23}	U_{13}	U_{12}
Pb(5)	47(2)	35(2)	34(2)	0(2)	4(2)	1(2)
Pb(6)	57(2)	31(2)	32(2)	-11(2)	3(2)	2(2)
Pb(7)	39(2)	53(2)	51(2)	-7(2)	-5(2)	-9(2)
I(1)	40(4)	196(14)	171(13)	3(7)	20(7)	-1(10)
I(2)	92(7)	68(4)	81(5)	5(4)	21(5)	38(4)
I(3)	138(10)	52(4)	68(5)	6(4)	0(5)	-17(3)
I(4)	49(5)	99(6)	100(6)	-16(4)	4(5)	2(5)
I(5)	106(8)	62(4)	89(6)	-5(4)	-11(5)	45(4)
I(6)	109(8)	55(4)	92(6)	-2(4)	-4(5)	34(4)
I(7)	32(4)	134(8)	127(8)	18(5)	10(5)	-4(6)
I(8)	97(7)	66(4)	81(5)	-7(4)	8(5)	-39(4)
I(9)	132(9)	59(4)	81(6)	8(4)	-2(6)	-34(4)
I(10)	27(3)	119(6)	106(6)	-13(4)	-4(4)	-14(5)
I(11)	120(8)	74(5)	75(5)	11(5)	6(5)	44(4)
I(12)	98(7)	64(4)	67(5)	-10(4)	-7(5)	35(3)
I(13)	39(3)	95(5)	104(6)	2(4)	5(4)	24(5)
I(14)	115(8)	72(5)	58(4)	9(5)	-6(5)	-33(3)
I(15)	88(6)	80(5)	62(5)	-10(4)	6(4)	-39(4)
I(16)	46(4)	78(4)	86(5)	-14(3)	-1(4)	11(4)
I(17)	104(7)	80(5)	56(4)	-1(5)	12(4)	-34(3)
I(18)	104(7)	80(5)	52(4)	1(4)	2(4)	-40(3)
I(19)	35(3)	105(6)	118(7)	25(4)	-1(4)	-1(5)
I(20)	148(10)	57(4)	61(5)	-3(4)	-9(5)	-21(3)
I(21)	106(8)	75(5)	64(5)	5(4)	-9(5)	-36(3)
I(22)	65(7)	189(14)	186(14)	-5(8)	-11(9)	-8(10)

The anisotropic displacement factor exponent takes the form: $-2\pi^2[h^2a^{*2}U_{11} + ... + 2hka^*b^*U_{12}]$.

Table S3. Pb-I Bond lengths [Å] for $(4AMP)(MA)_6Pb_7I_{22}$ at 293(2) K with estimated standard deviations in parentheses.

Label	Distances
Pb(1)-I(1)	3.086(12)
Pb(1)-I(2)	3.207(7)
Pb(1)-I(2)#1	3.169(8)
Pb(1)-I(3)	3.203(8)
Pb(1)-I(3)#2	3.181(7)
Pb(1)-I(4)	3.328(10)
Pb(2)-I(4)	3.121(10)
Pb(2)-I(5)	3.182(8)

Pb(2)-I(5)#1	3.180(7)
Pb(2)-I(6)#3	3.183(7)
Pb(2)-I(6)	3.154(8)
Pb(2)-I(7)	3.213(10)
Pb(3)-I(7)	3.163(9)
Pb(3)-I(8)	3.158(8)
Pb(3)-I(8)#4	3.189(7)
Pb(3)-I(9)	3.170(8)
Pb(3)-I(9)#2	3.170(7)
Pb(3)-I(10)	3.202(9)
Pb(4)-I(10)	3.153(9)
Pb(4)-I(11)	3.164(8)
Pb(4)-I(11)#3	3.180(7)
Pb(4)-I(12)	3.182(8)
Pb(4)-I(12)#1	3.163(7)
Pb(4)-I(13)	3.188(10)
Pb(5)-I(13)	3.170(10)
Pb(5)-I(14)	3.185(7)
Pb(5)-I(14)#2	3.157(7)
Pb(5)-I(15)	3.165(7)
Pb(5)-I(15)#4	3.188(7)
Pb(5)-I(16)	3.169(9)
Pb(6)-I(16)	3.213(9)
Pb(6)-I(17)	3.174(7)
Pb(6)-I(17)#2	3.165(7)
Pb(6)-I(18)#4	3.200(7)
Pb(6)-I(18)	3.166(7)
Pb(6)-I(19)	3.156(10)
Pb(7)-I(19)	3.239(9)
Pb(7)-I(20)#2	3.169(8)
Pb(7)-I(20)	3.205(8)
Pb(7)-I(21)	3.185(8)
Pb(7)-I(21)#4	3.204(8)
Pb(7)-I(22)	3.095(14)

Section S3. Additional calculation results.

In an apparent contradiction with experiment, our calculations show that the RP phase has a lower band gap as compared to DJ, with a difference amounting to ~80 meV, whereas the experimental data indicates a lower band gap for DJ (30 meV than of RP). Computed densities of states (Figure S3) confirm this trend. As already stressed, obtaining very precise structural information on high n-value members *via* X-Ray diffraction is challenging. Using the structure-property analysis based on two characteristic tilt angles (β, δ)[1] (Figure S2) allows to link the variation of the octahedral tilts to band gap variation. The experimental averaged tilt angles for BA and DJ are reported on the 2D map corresponding to the computed band gap variation with octahedral tilting in a Cs_2PbI_4 model structure. Figure S2 reveals that DJ has a slightly higher band gap as compared to RP, self-consistently with the calculated DFT band gaps obtained for the experimental n=7 structures. Noteworthy, for the n=1 member for which the structures are accurately determined, we recover the experimental trend, namely a lower band gap for DJ as compared to RP (Figure S4). Hence, we attribute the apparent discrepancy between the experimental and theoretical trends to both the quality of the structures as well as the difficulty of our DFT calculations to reach precisions below 0.1 eV for such large unit cells.
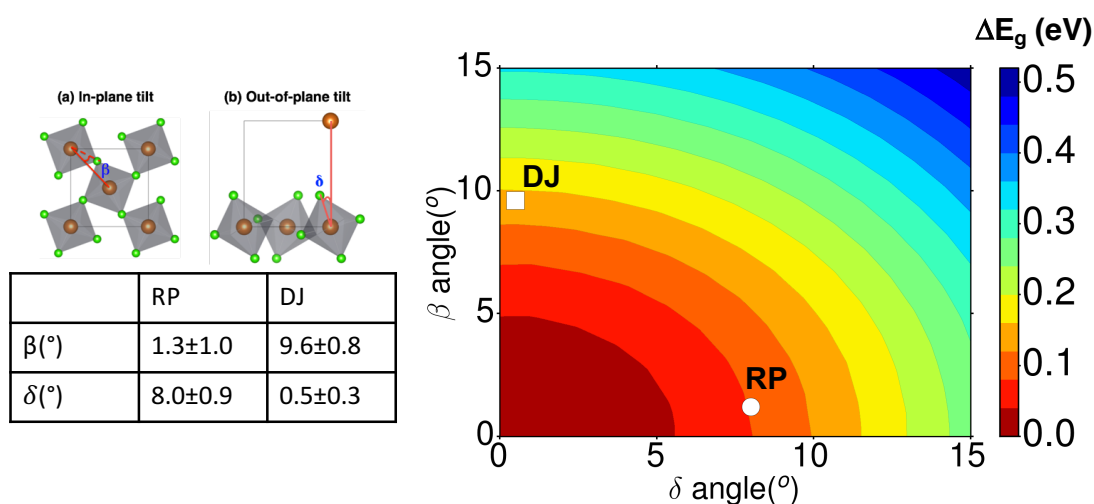

	RP	DJ
$\beta(°)$	1.3±1.0	9.6±0.8
$\delta(°)$	8.0±0.9	0.5±0.3

Figure S2. Band gap variation due to lattice distortion (β, δ) of the real DJ and RP structures plotted on the 2D map obtained for the n=1 Cs_2PbI_4 model structure[8].
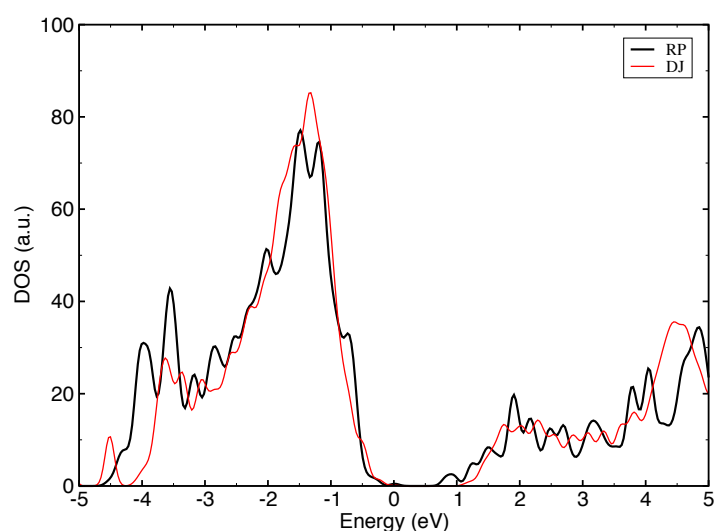

Figure S3. Density of States (DOS) computed without SOC for RP n=7 (black) and for DJ n=7 (red).
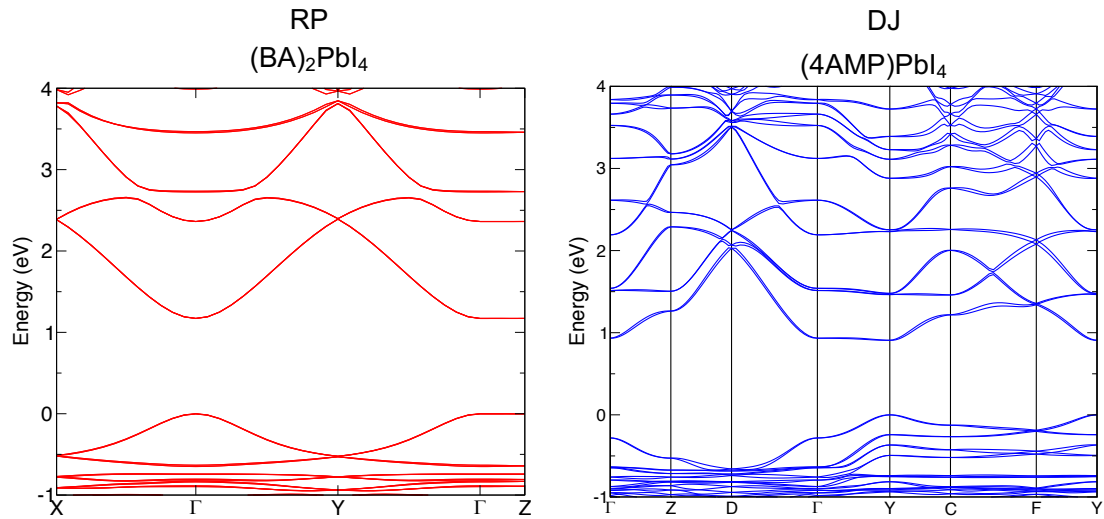
Figure S4. Comparison of the band structures of (left) $(BA)_2PbI_4$ and (right) $(4AMP)PbI_4$ including spin-orbit coupling. The calculated band gaps are 1.17 eV and 0.91 eV, respectively. Experimental structures have been taken from ref. 1 and ref. 2, respectively.
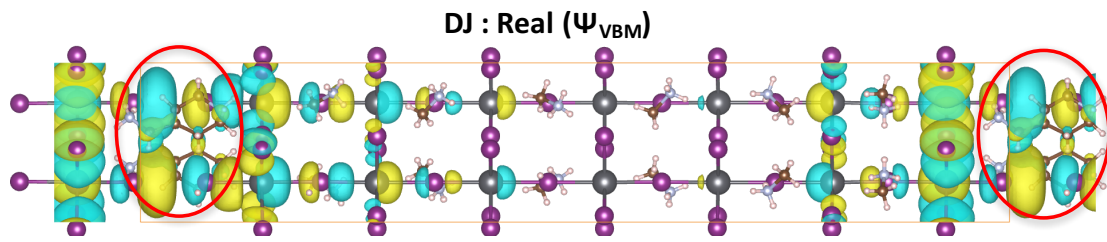
DJ : Real (Ψ_{VBM})

Figure S5. Wavefunction plot of the DJ compound without SOC at k-point (3/4 0 0) along ΓY direction. The circles show the anti-bonding hybridization between I...I atoms in contact with the 4AMP barrier layer.

RP

$(BA)_2(MA)_6Pb_7I_{22}$

DJ

$(4AMP)(MA)_6Pb_7I_{22}$

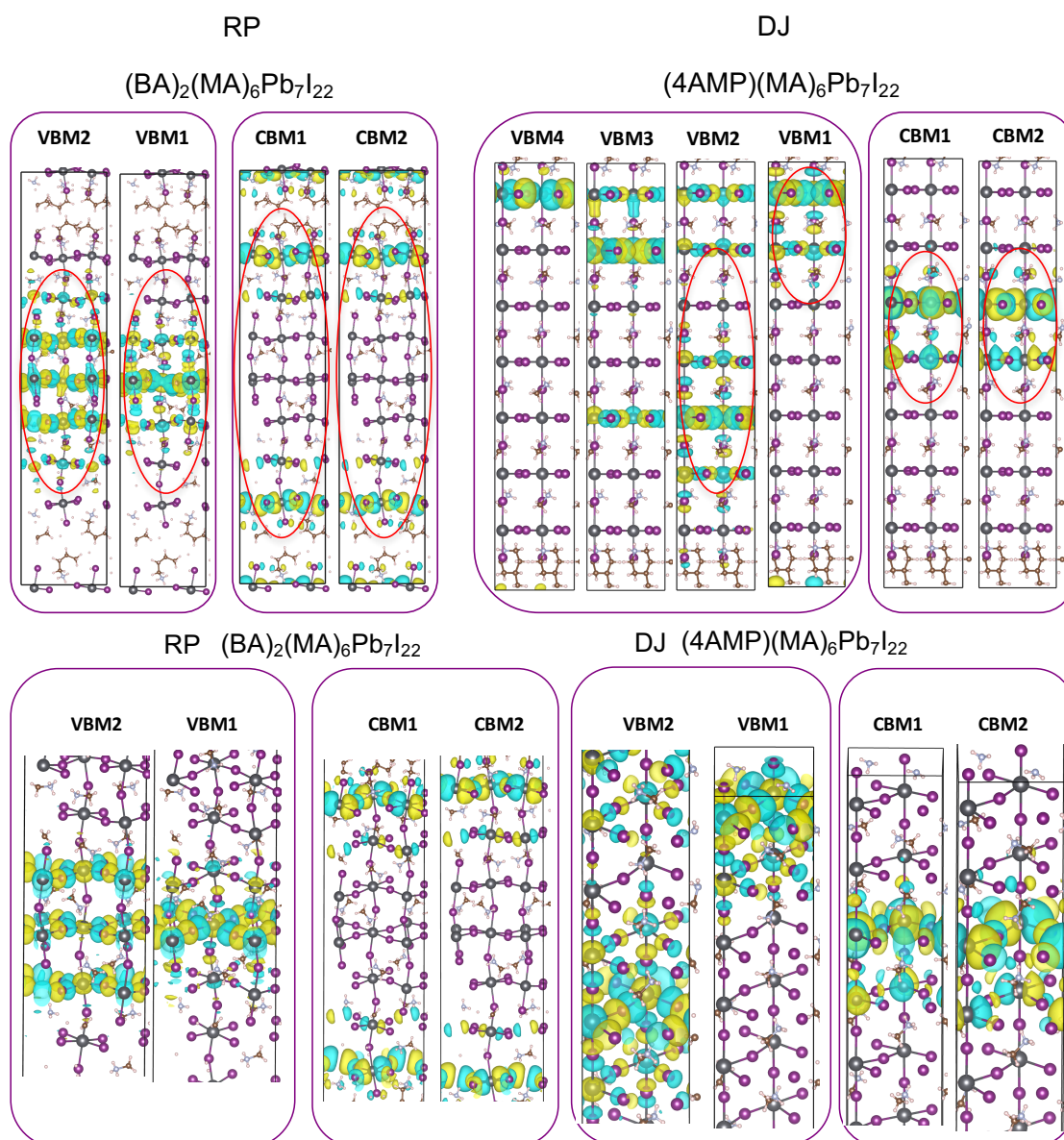RP $(BA)_2(MA)_6Pb_7I_{22}$

DJ $(4AMP)(MA)_6Pb_7I_{22}$

Figure S6. (top panel) Wave functions computed without SOC at (left) Γ for RP n=7 and (right) Y for DJ n=7. We note that for DJ, only the real part of the wave functions is plotted since the imaginary component also exists at Y. For RP, the wave functions being at Γ, no imaginary component exists. (bottom panel) The wave functions zoomed around circled area in the top panel.
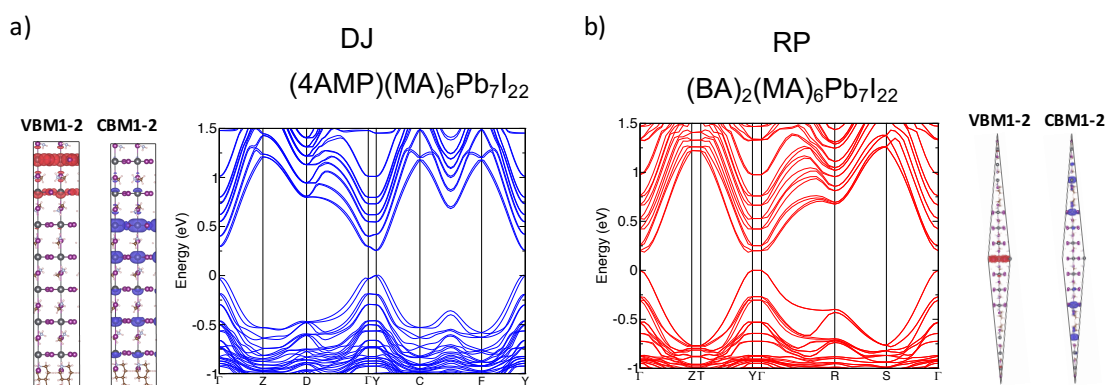
Figure S7. Band structures and local density of states (LDOS) with SOC for (a) the DJ and (b) RP compounds.

Possible dipole in the DJ compound

The particular orientation of NH_3 groups of MA cations pointing towards that of 4AMP indeed creates an important dipole in the unit cell. We first estimated this dipole using a slab calculation and it amounts to about 3.0 Debye. From the computed Hartree potential profiles of the structure, we extract an electric field of ~1.5 MV/cm in agreement with the one directly calculated using dipole correction of 3.0 Debye (Figure S8). Hence, these values are huge and are more than 5 orders of magnitude higher than the residual ones found numerically for the BA compound (Figure S9). We may thus infer from these calculations that the internal electric field promotes carriers' separation in the crystalline DJ compound. However, in thin films the random orientation of these dipoles most probably tend to significantly reduce these effects related to internal dipoles. Further experimental investigations are therefore requested to clarify this effect.
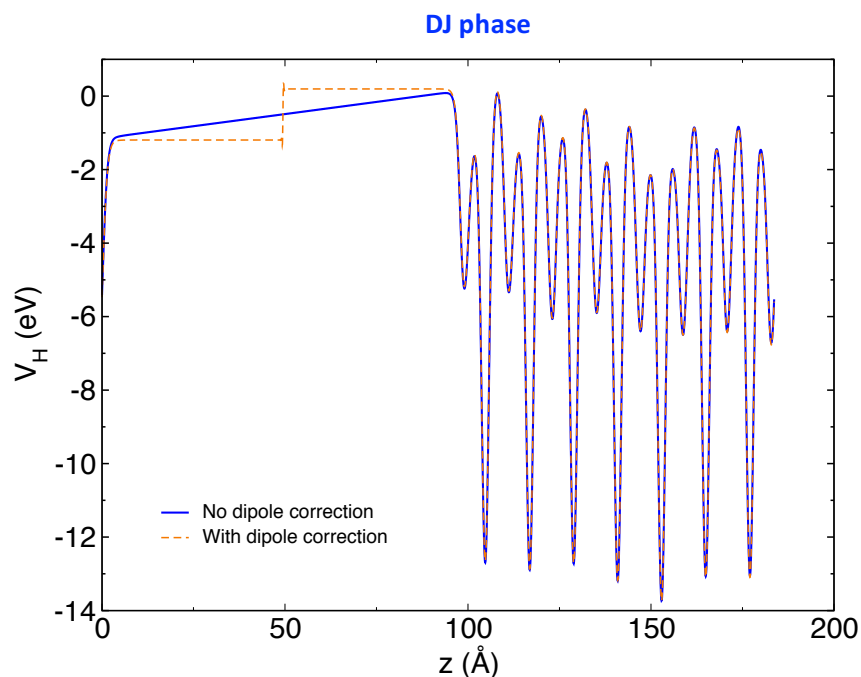

Figure S8. Hartree potential profile of the DJ compound. The slope of the uncorrected Hartree potential (blue) for the dipole in the vacuum region corresponds to the internal electric field.
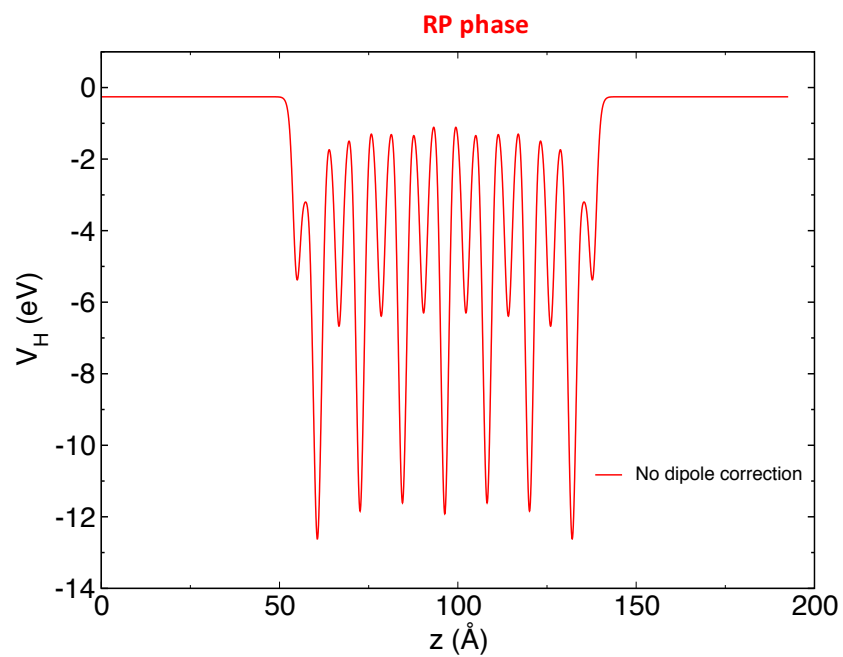
Figure S9. Hartree potential profile of the RP compound. As can be seen, no net dipole is present in the structure.

REFERENCES

[1]   L. Pedesseau, D. Sapori, B. Traore, R. Robles, H.-H. Fang, M. A. Loi, H. Tsai, W. Nie, J.-C. Blancon, A. Neukirch, S. Tretiak, A. D. Mohite, C. Katan, J. Even, M. Kepenekian, *ACS Nano* **2016**, *10*, 9776-9786.